Electrochimica Acta 217 (2016) 80–91

Contents lists available at ScienceDirect

Electrochimica Acta

journal homepage: www.elsevier.com/locate/electacta

Manganese oxide catalysts for secondary zinc air batteries: from electrocatalytic activity to bifunctional air electrode performance

Aroa R. Mainar[a,b,*], Luis C. Colmenares[a], Olatz Leonet[a], Francisco Alcaide[a], Juan J. Iruin[b], Stephan Weinberger[c], Viktor Hacker[c], Elena Iruin[a], Idoia Urdanpilleta[a], J. Alberto Blazquez[a,*]

[a] IK4-CIDETEC, P° Miramón, 196, 20014 Donostia-San Sebastián, Guipúzcoa, Spain
[b] Departamento de Ciencia y Tecnología de Polímeros, Facultad de Química, (UPV/EHU), P° Manuel de Lardizábal 3, 20018 Donostia-San Sebastián, Guipúzcoa, Spain
[c] Institute of Chemical Engineering and Environmental Technology, Graz University of Technology, Inffeldgasse 25C, 8010 Graz, Austria

ARTICLE INFO

Article history:
Received 9 June 2016
Received in revised form 7 August 2016
Accepted 9 September 2016
Available online 13 September 2016

Keywords:
Bifunctional air electrode
Secondary zinc-air battery
Manganese oxide based catalysts (Mn_xO_y)
Oxygen evolution reaction (OER)
Oxygen reduction reaction (ORR)

ABSTRACT

An efficient, durable and low cost air cathode with low polarization between the oxygen reduction reaction (ORR) and oxygen evolution reaction (OER) is essential for a high performance and durable secondary zinc-air battery. Different valence states and morphologies of Mn_xO_y catalysts were synthetized via thermal treatment of EMD (generating Mn_2O_3 and Mn_3O_4) and acid digestion of synthetized Mn_2O_3 (producing α-MnO_2) in order to develop an efficient Bifunctional Air Electrode (BAE). Change in the ratio H^+ to Mn_2O_3 during the acid digestion affects the sample microporosity, the crystallographic plane distribution, as well as the physical and chemical adsorbed water which was related to defects, *i.e.* cation vacancies (Mn^{4+}) and Mn^{3+}. These characteristics were discussed and linked to the electrocatalytic activity. The best ORR performing catalyst was that with the higher surface water content (associated to material BET surface area) and a (310) surface as the 2nd more contributing plane (after 211). On the other hand, the catalyst with the higher structural water and with (110) and (200) crystallographic planes being the most intensity contributors (after 211) was the most OER active material. In this work, it was able to find a relationship between catalyst structure and air-efficiency through a volcano-like relationship between air-efficiency and surface water content. Air-efficiency (also take as round-efficiency discharge/charge in battery context) can be taken as a good descriptor of potentially good materials for Zn-Air secondary batteries technology. In this term, we were able to prepare a Bifunctional Air Electrode based on the selected α-MnO_2 sample which demonstrated a round-efficiency of 53%, a ΔV around 1 V and a neglected loss of the charge potential (about 2.1 V) over the entire lifecycle test (more 200 cycles over 30 hours) with a capacity retention superior to 95%.

1. Introduction

The worldwide consumption of fossil fuels results globally in a dramatic increase of greenhouse gases in the atmosphere and locally in pollution of the air. When in future intermittent renewable sources like wind or solar radiation substitute fossil fuels, an efficient, safe and inexpensive energy storage systems will be required to store energy during production peaks and to supply energy according to the demands of the consumer [1].

In comparison to common rechargeable batteries such as lead-acid and Li-ion batteries, the metal-air batteries, especially secondary zinc-air batteries present low cost, low pollution, light weight, relatively high specific capacity/energy density, and they are generally considered as safe technology. However, the secondary zinc-air batteries, which normally are based on an aqueous alkaline electrolyte [2], are still under development due to the short cycle life of their electrodes [3].

Regarding the bifunctional air electrode, the large overpotential (ΔV) between the oxygen evolution reaction (OER) and the oxygen reduction reaction (ORR) reduces the cycle life limiting the performance of the secondary zinc-air batteries. Hence, the development of efficient and stable bifunctional catalysts towards the OER and ORR is critical to develop the technology [4].

* Corresponding author. Tel.: +34943309022; fax: +34943309136.
E-mail address: ablazquez@cidetec.es (J. A. Blazquez).

http://dx.doi.org/10.1016/j.electacta.2016.09.052
0013-4686/

The precious metals as platinum have been the most used catalysts for air electrodes but their high cost and scarcity limit their widespread applications in clean energy technology. The search for low cost catalysts with sufficient catalytic activity promoted the scientific interest in transition metal oxides as an alternative. Among them, manganese oxides (Mn_xO_y) exhibit promising electrocatalytic performances for OER and ORR under alkaline conditions and possess many advantages such as abundance in natural ores, low toxicity, low cost and environmental friendliness [5,6].

The performance of Mn_xO_y catalysts strongly depends on their morphologies, Mn valence state, preparation methods, crystalline phases and structures [7–12]. Mn_xO_y has over 30 different crystal structures and variable valences of Mn center in different polymorphs [13]. The different polymorphic forms with different properties include one-dimensional (1D) tunneled types (e.g. α-, β-, and γ-MnO_2), 2D layered compound (δ-MnO_2), and 3D spinel structure (λ-MnO_2).

The 1D structure differs in the arranged manner and size of the tunnels. Among them, α-MnO2 possesses both (2 × 2) and (1 × 1) tunnels surrounded by double binding octahedral chains. β-MnO2 consists of merely (1 × 1) tunnels separated by single chains, and γ-MnO2 displays (1 × 1) and (1 × 2) tunnels enveloped in double chains [7]. The alpha allotropic form is considered to be the most active. The superior performance of α-MnO_2 is attributed to the existence of different surface concentrations of Mn^{3+} ions, whose are supposedly higher and more accessible in this species than on the other allotropic forms of manganese dioxide [6]. It has been reported [7,14] that the polymorphic forms present ORR activities following the sequence: β-MnO_2 < λ-MnO_2 < γ-MnO_2 < α-—MnO_2 ~ δ-—MnO_2.

Although manganese oxides have been studied extensively, key factors that influence the specific ORR and OER activities are not well defined because it is not straightforward to compare across different studies [15]. Several methods have been developed for the synthesis of manganese dioxides [7,9,15–25]. Each technique results in considerably different crystallite/particle size [26], shape [7] and porosity [27]. Not only these properties affect the mass activity of the oxides, but also they correlate with the electronic structure at the surface and thereby give rise to different specific activities [15].

In this work, Mn_2O_3, Mn_3O_4 and α-MnO_2 catalysts with different morphologies have been obtained by relatively easy synthesis methods. The principal precursor used for the synthesis of the catalysts has been the electrolytic manganese dioxide (EMD). Heating this material reduces Mn to lower valence states, an effect that generally induces structural changes. Temperature between 625 °C and 725 °C promote the formation of Mn_2O_3 and between 950 °C and 1050 °C Mn_2O_3 is further transformed to Mn_3O_4 [28]. Different α-MnO_2 catalysts have been synthetized *via* acidic digestion from the as-prepared Mn_2O_3. The principal advantage of the acidic digestion synthesis method is the high purity of the final material. Typically, all other methods lead to a combination of different (*e.g.* structural, crystallographic) products reducing the purity of the targeting catalyst [29].

The synthesis of different α-MnO_2 in this work was based on changing the ratio of H^+ to Mn_2O_3 by incorporating different amounts of as-prepared Mn_2O_3 to a constant acid concentration. This is done with the intention of change the synthesis rate determinate step (disproportionation of Mn(III) into Mn(IV) and Mn(II) [29]) which could produce α-MnO_2 with different properties induced most likely by alteration in its morphology (variation of crystal growing rate). EMD and the generated catalysts (Mn_2O_3, Mn_3O_4 and α-MnO_2) were electrochemically evaluated and the results related to their physicochemical characteristics. The most promising materials in term of activity towards both ORR and OER were further investigated as Bifunctional Air Electrodes (BAE) in half-cell configuration assessing the bifunctional activity and the air-efficiency at a given current density. Finally, the most air-efficient material was incorporated as cathode in a lab-scale zinc-air rechargeable battery and the lifecycle assessed.

2. Experimental section

2.1. Synthesis of the Mn_xO_y catalysts

2.1.1. Generation of Mn_2O_3 and Mn_3O_4 from EMD

By means of a thermal method [30], Mn_2O_3 and Mn_3O_4 were synthetized from a commercial-grade electrolytic manganese dioxide (EMD). The Mn_2O_3 has been obtained by heating the EMD at 700 °C (heating rate of 5 °C min^{-1}) for 24 h in atmospheric air. On the other hand, when EMD was treated at 1000 °C (temperature ramp of 20 °C min^{-1}) for 2 h in atmospheric air, Mn_3O_4 was collected. Both resultant samples (Mn_2O_3 and Mn_3O_4) were left to cool down to room temperature in the furnace, and then crushed and stored in a desiccator. With the resulting Mn_2O_3 it has proceeded to the synthesis of α-MnO_2 *via* acid digestion.

2.1.2. Preparation of α-MnO_2 by acid digestion

All of the reagents used in this work are without further purification. The as-prepared Mn_2O_3 sample was used as precursor for the synthesis of different samples of α-MnO_2 *via* acid digestion. The acid digestion of Mn_2O_3 (*overall reaction*: $Mn_2O_3 + 2H^+ \leftrightarrow MnO_2\downarrow + Mn^{2+} + H_2O$) has been reported to follow a dissolution-precipitation mechanism [29,31] where the rate-determining-step (rds) is the disproportionation of Mn(III) into Mn(IV) and Mn(II) in electrolyte [29]. Through the solubility of the Mn(III) as intermediate and its disproportionation, the acid concentration and reaction temperature of the digestion play a crucial role in defining the phase of the MnO_2 (*i.e.* γ, α or β and/or a combination of them) as it can be observed in the phase diagram shown in Fig. 1 [32].

The kinetic transformation of Mn_2O_3 into MnO_2 has been regarded as an autocatalytic first order reaction ($\upsilon = k(X_A)(X_B)$; where k is the rate constant and X_A and X_B are the mole fractions of Mn_2O_3 and MnO_2, respectively) [31]. Hence, the additions of different quantities of Mn_2O_3 may change the rds for the overall process, and, in consequence, the α-MnO_2 properties obtained could be different. In this sense, following the last statement, the

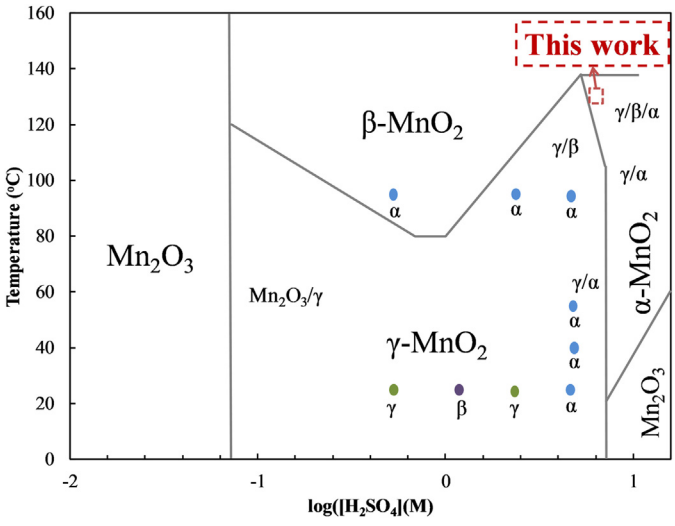

Fig. 1. Phase diagram resulting from the acid digestion of Mn_2O_3 [32].

synthesis of α-MnO_2 in this work was based on changing the H^+: Mn_2O_3 ratio by incorporating different amounts of as-prepared Mn_2O_3 but keeping the acid concentration constant. Thus, 3, 10, 13, 18 and 30 g of as-prepared Mn_2O_3 were correspondingly added to 1 L of 6 M H_2SO_4 (Scharlau, 98% purity) solution prepared with deionized distilled water (DDW), and kept under magnetic stirring for 16 h at 130 °C (see the zoom area marked in Fig. 1). After this time, the black precipitates were filtered and washed several times with ethanol and DDW. The resulting solids were dried overnight under vacuum and then dried 110 °C for 2 hour. The samples were cooling to room temperature in a desiccator and preserved there until use. Based on the amount of Mn_2O_3 precursor used in the acid digestion, the resulting α-MnO_2 samples are from now on labelled as α-MnO_2-3, α-MnO_2-10, α-MnO_2-13, α-MnO_2-18 and α-MnO_2-30.

2.2. Samples Characterization

2.2.1. Structural and morphological characterization

The phase composition of the Mn_xO_y samples was determined by X-ray diffraction (Bruker XS, D8 Advance equipped with Cu-Kα radiation). Each diffraction pattern was recorded in the 2θ range from 10° to 80° with a step size of 0.02° 2θ and a count time of 2 s per step. The crystallite size of the samples was calculated by Scherrer equation [33] taking the full-width-at-half-maximum (FWHM) of the main crystalline peak.

The morphology of each sample was examined using a Zeiss Gemini Ultraplus field emission scanning electron microscopy (FE-SEM) at various magnifications.

Surface water and structural water contents were determined following the procedure described in ref. 29. In brief, the surface water or physically bound water was determined by the weight loss of 500 mg of catalyst heated in an oven at 110 °C for 2 h in air. Further weigh loss of the sample by heating up to 400 °C for 2 h is attributed to the loss of chemically bonded water or structural water [34 and refs. cited therein].

Specific surface area was determined by applying Brunauer-Emmett-Tellet (BET) approach. Data was collected form N_2 physisorption using ASAP 2020 analyzer (Micromeritics, USA) recording the adsorption isotherms up to a relative pressure (P/P_0) of 0.3. Prior to adsorption the samples were outgassed at 150 °C (temperature ramp of 10 °C/min.) for 5 min and cooling down for 7 hours under vacuum.

2.2.2. Electrode preparation and Electrochemical measurements

The electrochemical characterization was performed by the well-known thin-film electrode using rotating disc electrode (RDE) and by half-cell Gas Diffusion Electrodes (GDE).

The thin-film working electrode (WE) was prepared by depositing a catalyst suspension on a glassy carbon (GC) substrate. The catalyst suspension was prepared mixing 9.8 mg of Mn_xO_y catalyst and 9.8 mg of carbon powder (Vulcan XC-72, Cabot Corp. to ensure electronic conductivity) in 5 ml of a solution isopropanol-water (7:3, v:v). The suspension was ultrasonically blended for 10 min. and then 10 μl of this suspension was carefully pipetted on the GC (0.196 cm^2) and left to dry by rotation at room temperature. The final thin-film working electrode yields 0.1 mg/cm^2 of catalyst (Mn_xO_y) loading.

Electrochemical measurements were performed in 0.1 M KOH electrolyte in a standard three-electrode cell at room temperature. The electrolyte was prepare from KOH (Sigma-Aldrich, 85% purity) dissolved in DDW. The thin-film WE was a RDE described above. Platinum wire and a commercial reversible hydrogen electrode (Gaskatel GmbH.) were used as counter and reference electrode, respectively.

For the ORR and OER, the RDE voltammograms were obtained in synthetic air (Air Liquide ALPHAGAZ 1 AIR; 20% O_2, 80% N_2; purity: 5.0) saturated electrolyte at 5 mVs^{-1} with a rotation rate of 1600 rpm. The WE's were cycled up to 5 times between OCV and 0.55 V for the ORR and between OCV and 1.6 V for the OER. The last cathodic sweep was used to evaluate the ORR activity via mass-transport correction. For the OER the last anodic sweep was used. The specific activity ($\mu A\ cm^{-2}_{oxide}$) is a practical approximation of the activity per active site, which is often unknown and reflects the intrinsic activity. This parameter is obtained by dividing the mass activity by the corresponding BET surface area leading to a characteristic property of the catalyst samples [15,35]. Thus, for both ORR and OER, Tafel plots were generated by plotting the logarithms of the BET surface area and mass specific normalized currents. Best performing catalysts were selected for further evaluation as GDE.

The GDE consisted of one active layer of air electrode prepared by mixing Mn_xO_y catalyst (40 wt. %), carbon nano-fiber (50 wt. %, made at TU Graz) and PTFE (10 wt. %, Dyneon TF 5032 PTFE) using isopropanol as solvent. The achieved Mn_xO_y catalyst loading was 8 mg cm^{-2}. The slurry was then rolled with Sigracet Carbon Paper as waterproof diffusion layer, and subsequently hot-pressed for 20 min at 20 kN and 290 °C to obtain the as-prepared bifunctional air electrode (BAE). The BAE working area is 1 cm^2.

Electrochemical test was carried out in 6 M of KOH (Sigma-Aldrich, 85% purity). Due to the high ionic conductivity, the commonly used KOH concentration in primary and secondary zinc-air batteries range between 6 and 8 M [2]. RHE from Gaskatel was used as reference electrode and a platinum wire as counter electrode in a three-electrode configuration glass cell. Electrolyte was saturated with oxygen by flowing synthetic air at 50 ml min^{-1} at room temperature. Pseudo steady-state-polarization-curves were galvanostatically obtained on a BaSyTec Test Cell System. The polarization curve (PC) was done 10 times in charge and 10 times in discharge modes. For both modes, BAE was initially kept at OCV for 15 min and then at 0.5 mA for another 15 min. Afterwards, the current was ramped as follow: ±0.5; ±1; ±10; ±40 and ±200 mA (with a cut-off voltage of 0.8 V or 1.8 V depending on the mode) for 8; 15; 5; 3 and 1 min, respectively, and then back to OCV to continue with the another mode and so untill complete 10 full charge/discharge cycles. This test was used to evaluate the bifunctional activity retention and air-efficiency of the BAE's. Stability was assessed comparing the third (3rd) and the tenth (10th) polarization curve. The first two PC's were used as BAE conditioning.

The bifunctional activity and the air-efficiency of the BAE were obtained at different current densities from the polarization curves. Bifunctional activity is defined as the voltage gap ($E_{OER} - E_{ORR}$) or overvoltage (ΔV) between charge(OER) and discharge (ORR) mode, while air-efficiency is taken as the ratio of ORR to OER ($[E_{ORR}/E_{OER}]$*100). It is also recognized as round-efficiency discharge/charge [36].

2.2.3. Battery performance measurements

Finally, the most efficient BAE was selected and tested under battery operating conditions. Thus, a GDE electrode of the selected material was prepared as explained above using CNF as conductive media. The battery consisted of a Zn-foil (50 μm) anode, a separator embedded with the supporting electrolyte (8 M KOH) and the GDE. Synthetic dried air was flowed at the cathode by means of 40 ml min^{-1}. The battery components were assembled in a commercial available ECC-Air cell (active area of 2.5 cm^2) from EL-CELL GmbH. Charge/discharge cycles (5 min/5 min) were performed at 10 mAh cm^{-2} and the capacity retention was assessed over the lifecycle test.

3. Results and discussion

3.1. Physical and morphological characterizations

The XRD pattern of the starting material (EMD) and as synthetized Mn_2O_3 and Mn_3O_4 are presented on Fig. 2. All XRD patterns are consistent with the corresponding assigned JCPDS card number, where no additional peaks could be observed, indicating the single-phase character of each sample. The heating procedure reduces Mn to lower valence states, an effect that generally gives rise to structural changes. Hence, the XRD patterns in Fig. 2 represent the phase change from EMD to Mn_2O_3 and subsequently to Mn_3O_4 by thermal treatment. The first (Mn_2O_3) corresponds to the reduction reaction $2MnO_2 \rightarrow Mn_2O_3 + 0.5O_{2(g)}$ at 700 °C and the second one (Mn_3O_4) corresponds to the reduction of $3Mn_2O_3 \rightarrow 2Mn_3O_4 + 0.5O_{2(g)}$ at 1000 °C. While EMD XRD pattern shows broad peaks, Mn_2O_3 and Mn_3O_4 samples display narrow and very sharp peaks indicating high crystallinity and larger crystallite sizes (3rd column in Table 1). The average of crystallite size was derived from Scherrer equation [37 and refs. cited therein] using the full-width-at-half-maximum (FWHM) of the diffraction peak (211). Mn_3O_4 shows almost a double crystal size in comparison to that for Mn_2O_3 as expected for sintered particles induced by the thermal treatment at temperature as high as 1000 °C.

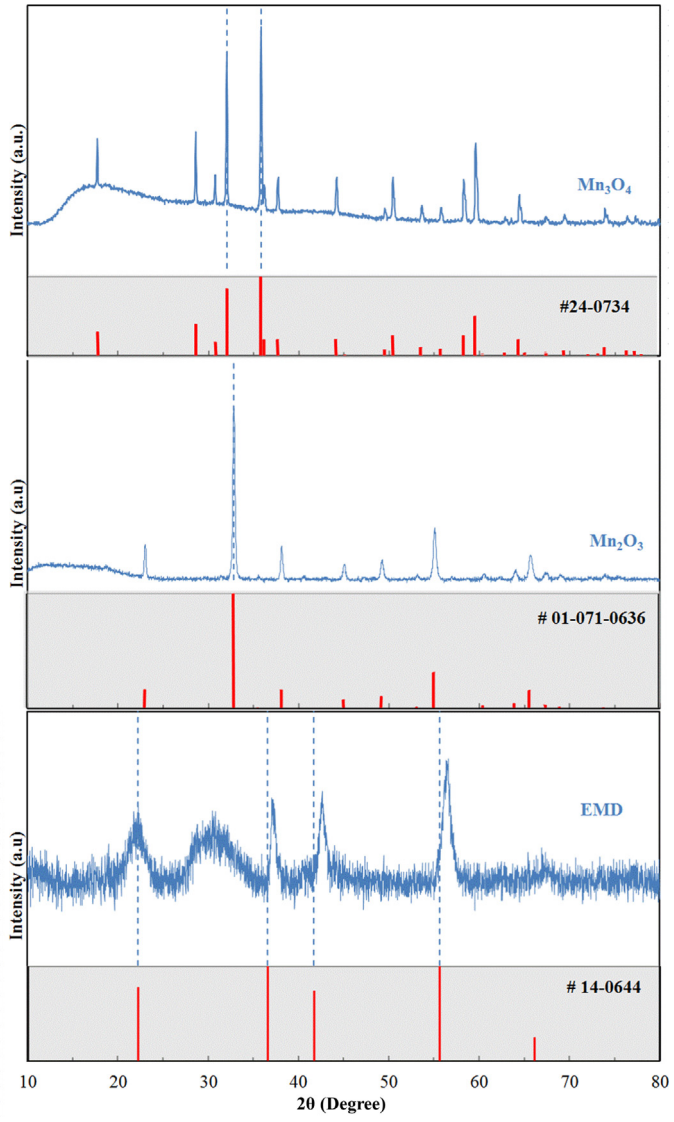

Fig. 2. X-ray diffraction patterns of precursor EMD and thermal synthetized Mn_2O_3 and Mn_3O_4 along with their corresponding JCPDS patterns.

The X-ray diffraction pattern of various α-MnO_2 samples derived from the acid digestion of Mn_2O_3 are shown in Fig. 3. All XRD pattern are very similar. It can be seen that all the reflections including the five characteristic peaks at 17.86°, 28.84°, 37.52°, 49.86°, and 60.27° (all of them contributing more than 50% of the intensity compare to 100% assigned to 37.52°) can be indexed to the body centred tetragonal α-MnO_2 (JCPDS No. 44-0141) indicating the phase pure of the synthetized α-MnO_2. Any reflections from precursor Mn_2O_3 can be apparently observed (see **Fig. S1** of ESI). However, a magnification of the XRD patterns between 2θ 54° and 58° (**Fig. S2** of ESI) shows for samples 13 and 20 a slight shift of peak (431) (for α-MnO_2) to the reflection peak (440) assigned to Mn_2O_3 (JCPDS No. 01-071-0636). Nevertheless, all α-MnO_2 samples are considered as phase pure. The crystallite sizes (3rd column in Table 1) obtained from the major diffraction peak (211) rank from 19.5 nm (α-MnO_2-20) to 43.5 nm (α-MnO_2-18) and not trends with the initial amount of Mn_2O_3 was observed.

Morphology of the samples was examined with FE-SEM. Figs. 4 (a-c) and 5 (a-g) show the micrographs of the different Mn_xO_y obtained in this work. Amorphous starting material EMD (Fig. 4**a**) presents flaky and porous morphology, while Mn_2O_3 powder obtained by heat treatment of EMD (Fig. 4**b**) has a reef-like morphology. It is mainly composed of micro-sized particles in the range 4.5–70 μm, constitute by quasi-spherical nano-sized particles. The micrograph reflexes the fact of sintered particles (in the range of 81.81 nm and 650 nm) by heating. This morphology has been also observed by Y. Park et al. [38] in the synthesis of $Na_{0.55}Mn_2O_4 1.5H_2O$ and $Na_4Mn_9O_{18}$ using Mn_2O_3 as precursor material. Denser non-porous smoothed boulder morphology is observed for the Mn_3O_4 sample (Fig. 4**c**).

Fig. 5**(a-g)** illustrates the micrographs for the as prepared α-MnO_2. The samples surface shape can be categorized as nano-flake, needle, rod and fiber/wire like morphologies. Hence, the micro-sized α-MnO_2 surface is influenced by the initial amount of Mn_2O_3 used during the acid digestion. Synthetized α-MnO_2-3 (Fig. 5**a**) presents smooth boulder particles in the range of 100 nm to 350 nm. This catalyst does not seem to consist of agglomerated nanoparticles, but nano-needles can be observed covering some of large particles. On the other hand, samples α-MnO_2-10; -13; -15; 18; and α-MnO_2-30 (Fig. 5-b; -c; -d; -e; and -g, respectively) consist of randomly dispersed nano-rod-like shape with different degree of agglomeration, lengths, widths, roughness and porosity. Finally, α-MnO_2-20 (Fig. 5**f**) presents a more like nanowire/fiber morphology. In all cases, it is clear that the materials obtained are appreciable homogeneous in their respective shapes. However, a clear relationship between initial amount of Mn_2O_3 and morphology cannot be noticed.

The BET surface area (SA) is a physical property which varies as function of the synthesis method or any sample treatment [3,39–41] which can affect e.g. the porosity or the surface roughness. Hence, BET surface area for the Mn_xO_y samples is shown in Table 1. As it can be seem, the BET SA of starting material (EMD with 34.15 $m^2 g^{-1}$) decreases in almost one order of magnitude (3.33 $m^2 g^{-1}$ for Mn_2O_3) or even closer to two orders (0.48 $m^2 g^{-1}$ in Mn_3O_4) by heat treatment at 700 °C and 1000 °C, respectively. As it was shown above, beside to induce phase changes, the thermal treatment also induces morphological changes (Fig. 4**a-c**) including the loss of SA by sintering. During this process the (micro)porosity practically disappears (see **Fig. S3** in ESI). For the as synthetized seven α-MnO_2 samples, the BET SA ranks from 13 to 67 $m^2 g^{-1}$. This large range of BET SA can be assigned to different micro and macro porosity amongst the samples which is not strictly related to the initial amount of Mn_2O_3

Table 1
Physicochemical characterization of Mn_xO_y samples.

Samples	BET ($m^2 g^{-1}$)	Cristal size (nm)	Surface Water (%)	Structural Water (%)	Water content (%)
EMD	34.15	N.A.	1.00	3.00	4.00
Mn_2O_3	3.33	32.5	0.23	0.09	0.32
M_3O_4	0.48	62.3	0.15	0.06	0.21
α-MnO2 -03	13.00	25.3	0.93	3.25	4.18
α-MnO2 -10	55.58	32.2	4.70	7.28	11.98
α-MnO2 -13	46.58	25.6	9.20	2.86	12.06
α-MnO2 -15	40.37	27.7	3.60	3.01	6.61
α-MnO2 -18	67.36	43.5	19.80	2.74	22.54
α-MnO2 -20	38.40	19.5	10.50	2.46	12.96
α-MnO2 -30	60.12	24.9	15.00	2.00	17.00

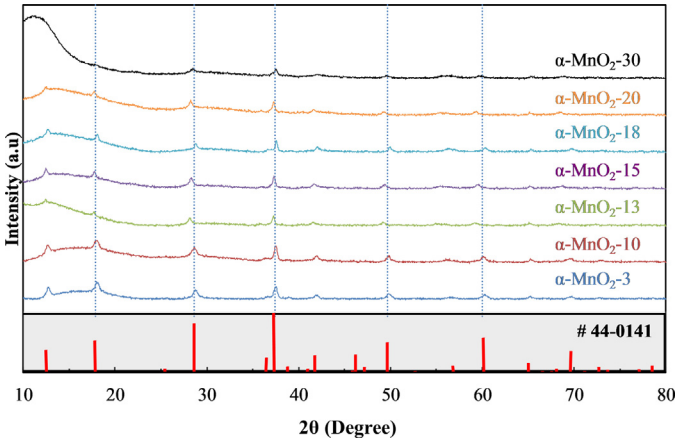

Fig. 3. X-ray diffraction patterns of α-MnO_2 synthetized via acid digestion of as-prepared Mn_2O_3. Respective JCPDS pattern is included as reference.

added to the acid media but to the rate of disproportionation of a soluble Mn(III) intermediate and precipitation of α-MnO_2. On the other hand, after α-MnO_2 formation, the excess of acid might also lead to some defects at the surface through etching process. Thus, both the BET surface area (Table 1) and the associated microporosity (region ≤ 0.3 p/p^o in the adsorption isotherm in **Fig. S3**) decrease in the sequent α-MnO_2–18 > 30 > 10 > 13 > 15 > 20 > 3.

In order to learn more about the structural defects in the synthetized samples, the surface and structural water content were determined for all samples [31]. In Table 1 the corresponding results of surface (physically bound), structural (chemically bound) and total water are shown for each Mn_xO_y sample. Surface water and, in general, the water content (surface plus structural water) decreases as the heat treatment temperature increases (EMD to Mn_2O_3 to Mn_3O_4) in line with the decrease observed in BET SA. It is explained by the fact that the amount of water absorbed on the surface or allocated in the pores and/or voids are determined by the available surface area, and hence, as expected, the water content is largely determined by the BET surface area of the material. This behavior is also, in general, observed for the α-MnO_2 samples. Among α-MnO_2 samples, No. 18 shows the high physically bounded water, while sample 10 presents the high content of structural water. However, it is noticeable that there is not direct relationship between water content and starting amount of Mn_2O_3 in the acid digestion processes.

Through the cation vacancy model [30,34], Ruetschi explained the relation between water content and electrochemical activity. He associated the structural water with both cation vacancies (Mn^{4+}) and Mn(III), i.e. with defects, and hence materials with significant amount of chemically absorbed water exhibits good electrochemical performance. The presence of structural water influences also other material properties such as density and electronic conductivity [34 and refs. cited therein]. Thus, on one hand higher defect content (structural water) favors the interfacial charge storage by increasing the electronic conductivity, and on the other hand, large porosity and higher content of physically (surface) bound water may facilitate the intercalation (protons or alkaline cations) process ($MnO_2 + H^+(M^+) + e^- \rightarrow MnOOH(M)$; M^+: Na^+, K^+, Li^+) [37], where water molecules reside in the (2 × 2) channels of the structure, which is the position normally occupied by intercalated cations [42]. In addition, taking into account the structural defects, Prélot et al. using the Pannetier structural model [43 and refs. cited therein] were able to explain with it the variation of the water dissociation constant of the surface sites at the interface solid-electrolyte, and thus local topography of the outermost oxide layers influence the properties of the first adsorbed water layer. Selvakumar et al. [41] have also demonstrated through their comparative study between α-MnO_2 catalysts with different morphologies (nanowire, nanotube, nanoparticles, nanoflower) that desorption of physisorbed and/or chemisorbed water molecules are largely influenced by the shape/morphology of the material. Thus, the authors have shown that structural water interacts stronger with e.g. α-MnO_2 nanotubes than with α-MnO_2 nanoflower. Thereby surface and structural properties (here represented by the BET surface area and surface and structural water) would influence the catalytic activity of materials towards the reduction and/or evolution of oxygen.

3.2. Oxygen reduction and evolution characteristics

The catalytic activity of the as prepared Mn_xO_y samples towards the ORR and the OER were assessed in air-saturated 0.1 M KOH electrolyte solution. The 5th ORR and OER lineal sweep voltammogramms (LSV) recorded at 5 mVs^{-1} under rotation rate of 1600 rpm are shown respectively in **Fig. S4** and **Fig. S5**. For the ORR, the mass-transfer corrected kinetic currents derived from the Koutecky-Levich equation along with the corresponding mass and catalyst BET surface area were used to obtain the kinetic current densities (J_k). Representing the Tafel plots from the J_k on different Mn_xO_y catalysts, the surface (Figs. 6**a**) and mass (Fig. 7**a**) specific activities at different potentials during the 5th LSV were accessed. Table 2 summarizes a comparison of the ORR surface (2nd column) and mass (3rd column) specific activities at 0.8 V_{RHE}. For OER, Tafel plots also illustrate the BET SA (Fig. 6**b**) and mass (Fig. 7**b**) specific activities. Column 4th and 5th in Table 2 shows the corresponding catalysts OER activity at 1.55 V_{RHE}.

The ORR proceeds on MnO_2 by two main routes: (*i*) the direct four-electron reduction pathway ($O_2 + 2H_2O + 4e^- \rightarrow 4OH^-$) and (*ii*) via the hydrogen peroxide pathway ($O_2 + H_2O + 2e^- \rightarrow OOH^- + OH^-$) which can be further reduce to complete the overall 4-electron ORR in alkaline medium. However, complete four-

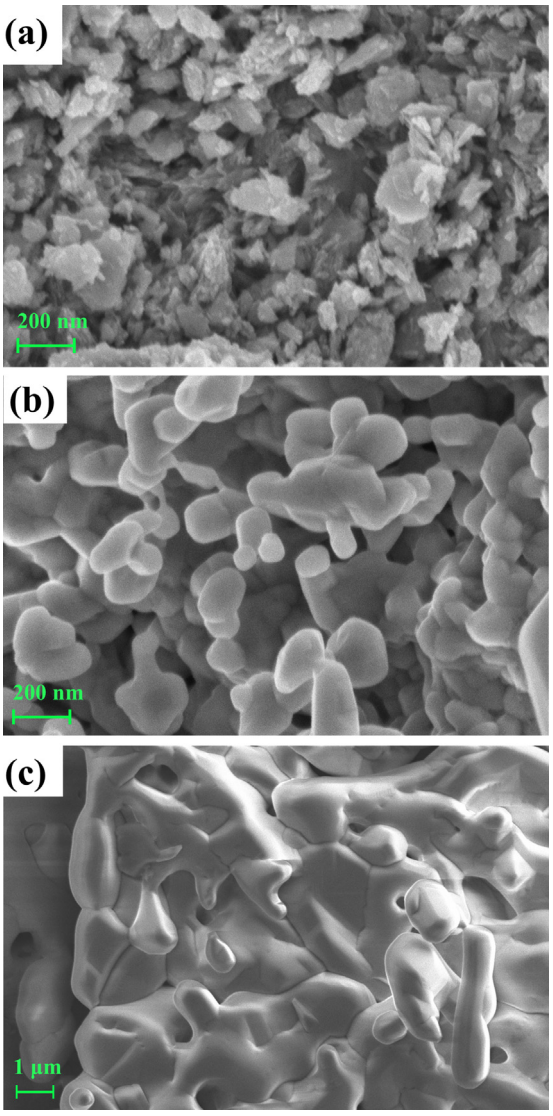

Fig. 4. FE-SEM micrographs illustrating the morphology of (a) EMD, (b) Mn_2O_3 and (c) Mn_3O_4.

electron reduction pathway is the most common pathway occurring on most crystallographic structures [6]. In both cases, the first step involves the conversion of manganese dioxide to manganese oxyhydroxide (MnOOH), on which the dissociative adsorption of molecular oxygen proceeds. The rate-determining step (rds) is the electron transfer to the adsorbed oxygen molecule in either the complete 4-electron reduction pathway or via the hydrogen peroxide 2-electron reduction pathway. K. Selvakumar et al. have demonstrated that on α-MnO_2 nanowires and nanorods (similar shapes to those shown in this study (Fig. 5)) are able to reduce oxygen via the direct 4-electron pathway on a single catalytic site due to its nano-geometry effect [41]. They found by DFT calculation that this direct ORR pathway is mainly associated to such of nanostructure which possesses active sites with two shortened Mn-O bonds along with an optimum required Mn-Mn distance which favors the adsorption of O_2 in a bridge-type interaction that conducts to dissociation of oxygen molecule and hence, the four electron reduction pathway. P.-C. Li et al. [3] have also confirmed that the ORR on nearly pure α-MnO_2 catalysts proceeds via 4-electrons. In his case, it was explained by a sequential (serie) two-electrode pathway or so called quasi-4e reduction pathway (see refs. cited in ref. 3) due to the ability of MnO_2 to disproportionation of HO_2^- into OH^- and O_2. Based on these facts, and since the samples synthetized in this work present mainly a nanorod shape, it has assumed that the reduction of oxygen on as-synthetized α-MnO_2 samples proceeds via 4-electron pathway where H_2O_2 generation could be neglected at the potential of interest.

As it can be observed in the comparative Table 2, α-MnO_2-18 for the ORR and α-MnO_2-10 for the OER are the most active catalysts among the synthetized materials and even better performing than those activities reported in the literature for other kind of α-MnO_2 catalysts [7,10,12,44]. In case of the investigated α-MnO_2-18, the mass activity achieves about 15 $A\,g^{-1}{}_{ox}$ at 0.8 V_{RHE} which is outperforming the best published catalyst based on α-MnO_2 [44].

Mn_2O_3 and Mn_3O_4 catalysts present very low ORR activity compared to the α-MnO_2 catalysts (Fig. 7**a**). The (2 × 2) tunnel structures (α-MnO_2) were proven to have higher intrinsic activities over layered materials, considering the accessibility of water and the defects by these two systems [12]. For MnO_2-based catalysts, it has been demonstrated that the ORR activity follows an order of α- > β- > γ-MnO_2, which is attributed to a combinative effect of their intrinsic tunnel size and electrical conductivity. On the other hand, MnO_2 catalysts with the same phase, the nanostructures apparently outperform the micro-sized particles due to smaller size and higher specific surface areas. Other possible reason is associated to the nature of preferentially exposed plane of manganese oxides [45].

Recently J. Liu et al. [46] has shown a significantly ORR enhancement on morphological tailored Mn_3O_4 catalysts. By synthetizing Mn_3O_4 with small nanoparticles (NP-S), large nanoparticles (NP-L), nanoflake (NF) and nanorod (NR) morphologies the authors were able to achieve 16.4 $A\,g^{-1}{}_{ox}$ at 0.83 V on NP-S Mn_3O_4. In the same kind of idea, but only apply to α-MnO_2 crystallographic form, K. Selvakumar et al. [40] developed shape-engineered (nanoparticles (NP), nanowires (NW) and nanotubes (NT)) α-MnO_2 as bifunctional ORR/OER catalyst. They found NW-shape as the best performing towards both ORR and OER. This result was explained by the associated surface energies and adsorption of water on the surface, where the shape of the material largely influenced the physically (surface) and chemically (structural) bounded water. Both groups [40,46] pointed out the remarkable shape effect on the ORR activity for Mn_xO_y based catalyst, as well as, with the help of density functional theory (DFT), the correlation between enhanced ORR activity and preferentially exposed planes (001 for NF Mn_3O_4 [46] and 310 for NW α-MnO_2 [40]).

K. Selvakumar and co-workers [40] have calculated by DFT that (310) and (200) surfaces in α-MnO_2 are strongly interacted with water molecule, while the (110) surface is weakly bonded with the adsorbate due to its high structural stability. In the case of (211) plane, it is expected to have high catalytic activity. This crystallographic plane is the dominating surface for all α-MnO_2 catalysts as it is shown above in Fig. 3 and in **Table S1** (ESI). However, for α-MnO_2-18 and α-MnO_2-10 the second dominating plane is the (200) with the different that in sample 10 the (110) surface intensity contribute almost in the same proportion than (200) and even more than (310), while in sample 18 this plane (110) intensity contributes about 18% and 12% less than that for (200) and (310), respectively. For the other α-MnO_2 materials, (310) plane is the second more predominating intensity, being that more remarkable on sample 13 and 20 (almost 20% over the (200) surface and about 30% respect to plane (110) for both catalysts). In α-MnO_2-3 that different between 310 and 200 is just 7%, while (110) surface intensity is about 20% less intense than (310) in its XRD pattern. Interestingly to notice is the almost similar intensities of planes (110), (200) and (310) in α-MnO_2-15. This sample, spite to show a relative large BET surface area (40.37 m^2g^{-1}) which is very

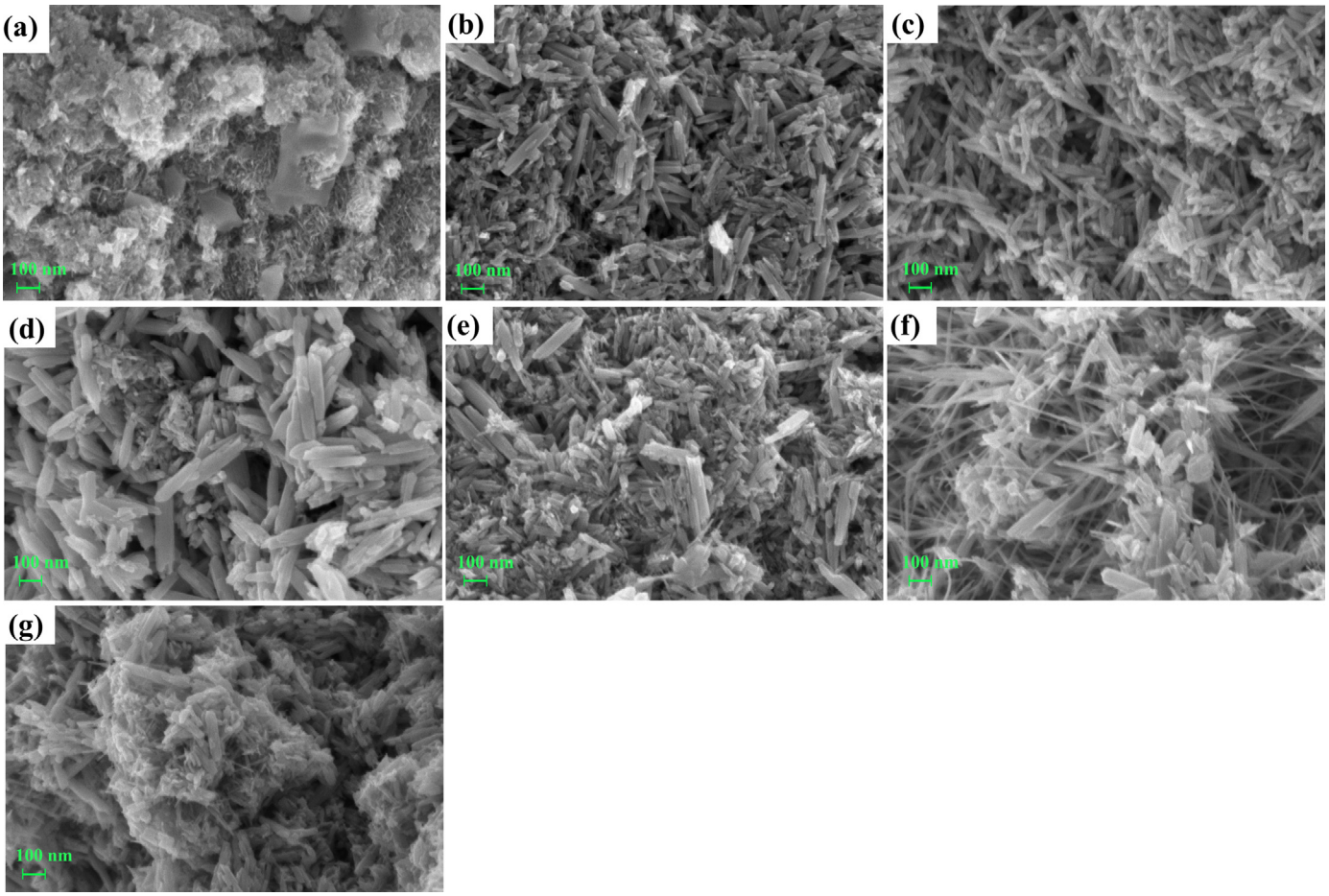

Fig. 5. FE-SEM micrographs illustrating the morphology of different α-MnO_2 synthetized *via* acid digestion of Mn_2O_3: (a) 3; (b) 10; (c) 13; (d) 15; (e) 18; (f) 20 and (g) 30.

close to *e.g.* samples 13 (46.58 $m^2 g^{-1}$) and 20 (38.40 $m^2 g^{-1}$), this material has resulted in the less active α-MnO_2 catalysts towards the ORR (with exception of sample 10) and OER, whilst α-MnO_2-13 and 20 have shown a similar and promising bifunctional activity. Based on these facts, and in addition, as Table 1 shows, α-MnO_2-18 is the catalyst with most large amount of surface water (about 20%), as well as the material with the larger BET surface area. The direct correlation water surface and ORR performance is largely linked to the mass specific kinetic ORR activity instead BET surface area. As it can be seem in Tables 1 and 2, the surface water and the mass specific kinetic ORR activity varies almost in the same sequent while BET surface area normalized kinetic current might be influenced by the corresponding crystallographic plane distribution.

On the other hand, α-MnO_2-10, the most OER active catalyst (Figs. 6 b and 7 b) amongst the synthetized materials, presents the higher structural water content (Table 1) with (110) and (200) crystallographic planes being the most intensity contributors after the common dominating (211) plane (**Table S1**). In order to compare the OER catalytic activity, other α-MnO_2 catalysts reported in literature are also included in Table 2. Y. Meng et al. [12] reported the specific and mass OER activities at 1.679 V_{RHE}. In this work the catalysts were not exposed to higher potentials than 1.6 V_{RHE} because the binder free catalysts layer may detach at higher voltages due to gas evolution. In this context, the current densities at 1.60 V_{RHE} are provided.

As fallows, the crystallographic plane distribution (in term of intensities) observed in **Table S1** and realized above, as well as the sample water content (surface and structural) could be both associated to the observed trends for ORR and OER activities among the synthetized α-MnO_2 samples. In this sense, the catalyst activity could be related to the structural/surface defects created during the acid digestion of Mn_2O_3 [32] for the morphological (nanorod/tube/wire as observed in Fig. 5) similar synthetized α-MnO_2 samples. Thus, higher defects (mainly cation vacancies – related to structural water) can be produced when crystallite growing/precipitation rate is quicker. The latter is accelerated by increasing acid concentration (H_2SO_4) which leads to larger crystallites and the already mentioned defects within MnO_2 structure [32][32 and refs. cited therein].

The results showed in Table 2 and Figs. 6 and 7, corresponding to the 5th cycle (stable LSV), indicate that there is not one unique good α-MnO_2 catalyst for both oxygen reduction and evolution reactions. It should be mentioned here, that ORR and OER activity assessment was done on the stable LSV. The slight difference between the first and the fifth cycles are reported in **Fig. S6**. Such kind of difference can be associated to conditioning of the samples by removing residual chemicals from the ink and/or partial electrochemical oxidation of the carbon used as conductive medium (50 wt.% of the composite) which may contribute to the overall Faradaic current. It cannot be rule out partial deactivation of the samples by formation of less ORR active surface species such as MnOOH [3] or Mn_3O_4 [47][47 and refs. cited therein].

It should point out that the main objective of this study is to investigate the applicability of α-MnO_2 as cathode catalyst in air-electrodes under simulated Zn-air secondary battery test conditions rather than investigate in depth the intrinsic properties of the α-MnO_2 samples. In this term, the main focus in the following

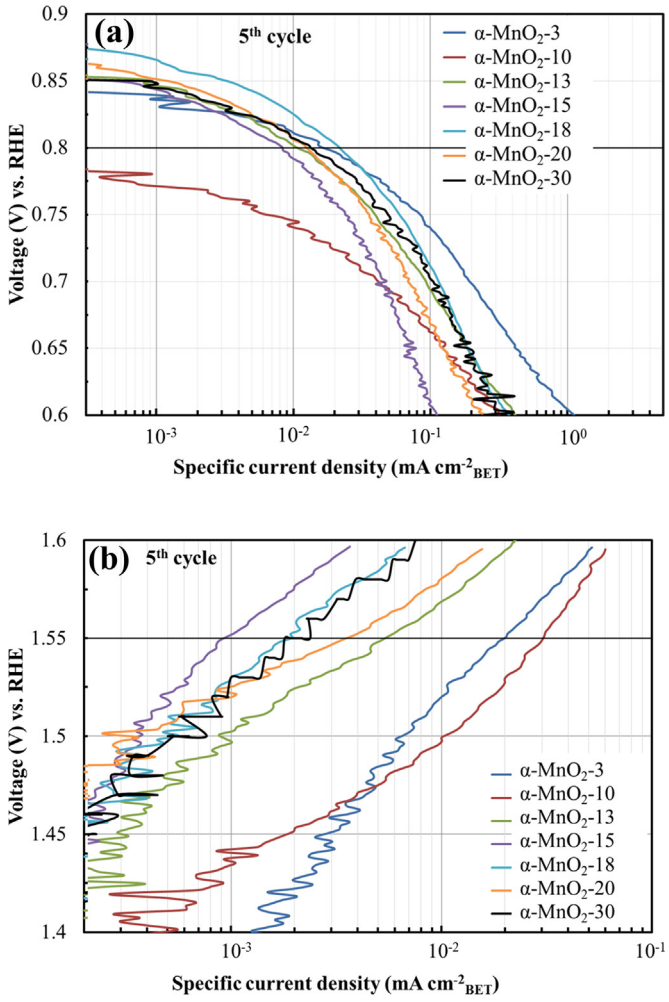

Fig. 6. BET surface area normalized ORR kinetic currents (a) and OER currents (b) of synthetized α-MnO_2 catalysts in air-saturated 0.1 M KOH. Scan rate: 5 mV s^{-1}; 1600 rpm.

sections is the search of an effective electrode with good bifunctional activity towards ORR and OER and good air-efficiency. The bifunctionality is measured in term of voltage gap or overpotential ($\Delta V = E_{OER} - E_{ORR}$) between charge(OER) and discharge(ORR) mode, and in term of air-efficiency taken as the ratio of ORR to OER ($[E_{ORR}/E_{OER}]^*100$) at a given current density in both cases. In order to do that, Gas Diffusion Electrodes were manufactured with the selected (10, 13, 18, and 20) α-MnO_2 catalysts and compared to the starting sample Mn_2O_3 as well as against Mn_3O_4 material.

3.3. Electrochemical assessment of the Bifunctional Air Electrode (BAE)

BAE for automobile application, for example, must support fast potential changes induced by the battery discharge during acceleration (high power demand) followed by charge phase during regenerative braking. In ideal conditions all the components of the electrode should withstand such conditions. In this sense, a bifunctional catalytic monolayer configuration could be the most efficient and cost effective design [36]. Taking into consideration efficiency and cost, single catalytic layer of selected α-MnO_2 catalysts were manufactured into a BAE. As-prepared Mn_2O_3 and Mn_3O_4 were also tested for comparison. Since the metal oxide based catalysts present in general low bulk conductivity, the Mn_xO_y-based catalyst inks were prepared using 50 wt.% carbon nanofibers (CNF) as conductive media. The use of carbon in BAE has been controversial due to its electrochemical oxidation at oxygen evolution potentials. However, carbons with higher graphite character [48] and/or nanostructured (such as nanofiber, nanotube, etc.) have shown better resistance towards the corrosion, and have been used as part of cathode electrodes. P.-C.Li et al. [3] have found a ratio carbon (XC72) to α-MnO_2 of 1 as the optimal in term of ORR performance. Furthermore, addition of carbon in the catalyst composite provides better control of the electrolyte permeability within the hydrophilic catalyst layer due to the change in permeability [49,50] helping to achieve optimal electrolyte and oxygen permeability and hence, provide an extended reaction zone at the three-phase boundary [36].

Chronopotentiometric measurements at different current densities were carried out on the as-fabricated BAE to assess their bifunctional activities (in term of overpotential, ΔV) and air-efficiency over a short-term test (10 galvanostatic measures at both ORR and OER, meaning of 20 polarization curves (PC) in total). Fig. 8 represents the third ORR/OER polarization curves (first two cycles were taken as conditioning of the electrodes), whilst Fig. 9 summarizes the retention of bifunctional activity (Fig. 9**a**) and air-efficiency (Fig. 9**b**) at 20 mA cm^{-2} (pointed by the segmented red line in Fig. 8) over the short-term stability test.

As it can be observed in Fig. 8 there is not apparent difference in the ORR/OER polarization curves among tested catalysts. However, as Fig. 9**a** and **Table S2** show, α-MnO_2-13, −18 and −20 have outstanding bifunctional activities with ΔV as lower as almost 0.7 V for low current densities (at the initial state, 628 mV for α-MnO_2-13 at 5 mA cm^{-2}) or around 0.8 V ΔV for intermediate current densities. P.H. Benhangi and co-workers have recently reported an ORR-OER potential window (ΔV) of 662 mV for MnO2 catalyst at 2 mA cm^{-2} being 563 mV the lowest ΔV reported for activated MnO2-$LaCoO_3$ [47]. They have also cited 650 mV ΔV for Pt/IrO_2 (a nobel metal based material) and 866 mV for Mn_2O_3, whereas here reported Mn_2O_3 showed a improved performing with 689 mV at 5 mA cm^{-2} and 856 mV at 20 mA cm^{-2}.

On the other hand, as it observed in Fig. 9**a**, α-MnO_2-13 catalyst shows the best bifunctional retention (97.7%) among the α-MnO_2 samples. This bifunctional activity retention was similar to that shows by Mn_2O_3 but slightly lower that the 98.8% obtained by Mn_3O_4 catalyst. This high retention of Mn_2O_3 and Mn_3O_4 could be related to the stability of their ceramic-like morphology (low BET surface area and porosity) for both catalysts, induced by the EMD thermal treatment and hence, not significant morphological/structural changes are expected for these materials with the fast potential variations during charge/discharge cycles. This assumption could be corroborated by postmortem analysis (not performed in this work but intended for ongoing activities).

In order to go deeper into the functionality of the tested materials, Fig. 9**b** illustrates the catalysts air-efficiency (ORR/OER ratio at 20 mA cm^{-2}) and its variation after the short-term stability test (**Table S3** summarizes the air efficiencies values at the 3rd (initial state) and after 10 PC's for comparison and retention assessment). Similar to what has occurred with ΔV, α-MnO_2-13, −18 and −20 have shown the best air-efficiency. At the initial state (3rd cycle) they present (**Table S3**) a respectively efficiency of 59.2%; 58.0% and 59.0% at 5 mA cm^{-2} and correspondingly 46.9%; 46.8% and 47.3% at high current density (40 mAcm^{-2}). Among them, α-MnO_2-13 was the only one able to keep a reasonable air-efficiency (46.1%) at 40 mA cm^{-2} after cycling. This catalyst has demonstrated superior (about 98.8%) air-efficiency retention (Fig. 9**b** at 20 mAcm^{-2} and **Table S3** for all current densities) in comparison to the other α-MnO_2 samples (98.3% for sample 18 and 96.8% for sample 20, both at 20 mA cm^{-2}). Therefore, it was choose as cathode for the battery tests.

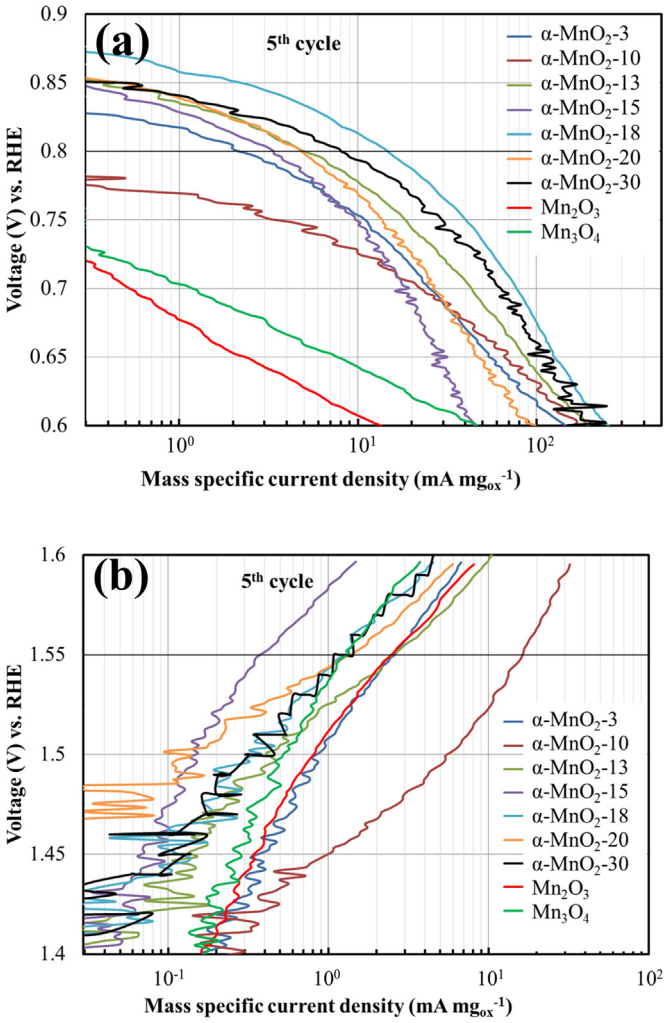

Fig. 7. Mass specific normalized ORR kinetic currents (a) and OER currents (b) of synthetized α-MnO_2; Mn_2O_3 and Mn_3O_4 catalysts in air-saturated 0.1 M KOH. Scan rate: 5 mV s^{-1}; 1600 rpm.

In general, the loss of bifunctional activity and air-efficiency can be associated to the formation of Mn_3O_4 which has been recognized as the reason of the lower rechargeability of manganese oxide since it cannot be electrochemically oxidized to active MnO2 during cycling [47 and refs. cited therein]. This will also partially explain the high retention of ΔV and the lower loss of air-efficiency for Mn_3O_4 sample, although its performance is always lower compare to more active α-MnO_2 materials.

Fig. 10 illustrates the relationship between catalyst structure and air-efficiency. The segmented lines represent the trend at the initial state (3rd cycle) and the solid lines after 10 PC's. As it can be observed this relationship goes through a maximum (around 10%) describing a Volcano-like plot at each current density. The maximum is achieved by samples α-MnO_2-13 and α-MnO_2-20, having both catalysts a comparable surface water content (Table 1) and air-efficiency (**Table S3**).

In Section 3.3, water content was associated to the ORR/OER activity through the surface and structural defects. As it was pointed out, K. Selvakumar et al. [40] demonstrated with the support of experimental data and DFT calculations that the good performing of α-MnO_2 towards both ORR and OER can be correlated with surface energies and adsorption of water on the surface. Furthermore, the shape of the material will largely influence the surface and structural bounded water. The authors have calculated by DFT that (310) and (200) surfaces in α-MnO_2 are strongly interacted with water molecule, while the (110) surface is weakly bonded with the adsorbate due to its high structural stability. This property indicates that the nature of preferentially exposed facets of manganese oxides would be another influential factor [45] that may address the material reactivity. As it can be assumed this relationship among exposed facet-water content-activity would also induce a volcano trend. This trend is reflected in Fig. 10 where sample 13 and 20 have the best balance and hence, the optimal relationship. Both samples have (310) surface as the dominating plane after the main common (211) surface. They also showed a similar surface and structural water content. Although sample 10 also have the similar total water content (about 12%) than them, this sample does not shown a dominating plane among (110), (200) and (310), thus its interaction water-surface-activity is different than that for α-MnO_2-13 and α-MnO_2-20, being its relationship air-efficiency-surface water at the left side (weak interaction) of the volcano-like plot (Fig. 10). In the case of α-MnO_2-18, the dominating surface after (211) is the plane (200). The sample showed huge surface water content and in overall the larger total water content (22%) among α-MnO_2 samples. With this structural/surface property its relationship air-efficiency and surface water is at the right side (i.e. strong interaction with water) of the volcano-like plot.

Table 2
Comparison of the ORR (0.8 V_{RHE}) and OER (1.55 V_{RHE}) surface specific and mass specific normalized currents.

Sample	$J_{k(0.8V)}$ (μA cm^{-2}_{BET})	$J_{k(0.8V)}$ (A g^{-1}_{ox})	$J_{1.55V}$ (μA cm^{-2}_{BET})	$J_{1.55V}$ (A g^{-1}_{ox})	Reference
Mn_2O_3	–	–	–	2.41	This work
Mn_3O_4	–	–	–	1.33	This work
α-MnO2 -03	16.07	2.09	20.17 (51.9*)	2.62 (6.8*)	This work
α-MnO2 -10	–	–	30.19 (60.1*)	16.18(32.2*)	This work
α-MnO2 -13	10.49	4.89	5.55 (22*)	2.58 (10.6*)	This work
α- MnO2 -15	8.36	3.37	0.96	0.38	This work
α- MnO2 -18	21.94	14.78	1.95	1.31	This work
α- MnO2 -20	12.48	4.79	3.43	1.32	This work
α- MnO2 -30	13.40	8.06	1.80	1.08	This work
α-MnO_2 (nanorod_SF)	6 (147 m^2g^{-1})	8.8	–	–	[44]
α-MnO_2	6.4 (112 m^2g^{-1})	7.2	20.89**	23.40**	[12]
α-MnO_2-HT	– (67 m^2g^{-1})	–	26.41**	17.7**	[12]
α-MnO_2/C	10 (8 m^2g^{-1})	0.8	–	–	[7]
α-MnO_2 (nanorod)	2 (19.5 m^2g^{-1})	0.39	–	–	[10]
α-MnO_2 (nanotube)	1 (26 m^2g^{-1})	0.26	–	–	[10]

* At 1.6 V_{RHE}.
** At 1.679 V_{RHE} (converted potential).

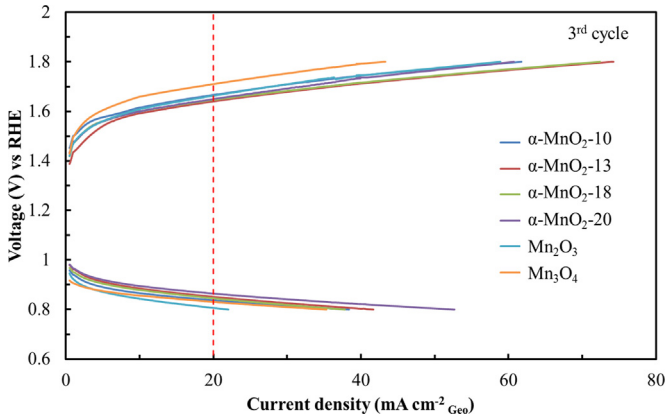

Fig. 8. Resulting galvanostatic polarization curves (3rd curve) for Bifunctional Air Electrodes prepared with selected Mn_xO_y catalysts in air-saturated 6 M KOH. Air flow: 50 ml min^{-1} at room temperature.

3.4. Battery performance of BAE under relevant Zn-Air operating conditions

Fig. 11 shows the reversibility of a zinc-air full cell battery containing the catalyst α-MnO_2-13 as cathode. This test validates the use of as-synthetized α-MnO_2 catalyst and carbon (CNF as conductive media) as a suitable BAE under relevant Me-air battery conditions. A zinc foil with 50 microns thickness has been employed as anode and standard 8 M KOH embedded in the separator as aqueous alkaline electrolyte. The test consisted in a continuous charge/discharge cycle at 10 mAh cm^{-2} at room temperature.

As it is represented in Fig. 11 the full battery cell system shows an OCV of 1.42 V (1.44 V in ref. 3), more than 30 hours of operation, and a good reversibility even after 200 charge/discharge (C/D) cycles, maintaining along the test more than the 95% of the initial capacity (red dotted line in Fig. 11). As the magnification inside Fig. 11**a** shows, the system presents the classical charge/discharge profiles with an overpotential (ΔV) around 1.0 V and a round-efficiency C/D about 53%. From about 175 cycles is observed a slight capacity loss (red dotted line in Fig. 11), however, the ΔV (different between both solid green lines) stays unaffected (Fig. 11**b**). This loss of capacity but stable ΔV might be interpreted as a loss of accessible zinc active material at the anode and/or dried conditions in the cell provoked by water consumption (included water evaporation) which limited the lifecycle of the battery. In addition, stable potential observed during the charging phase over the lifecycle (more than 200 cycles) is also a good indication of the excellent BAE stability.

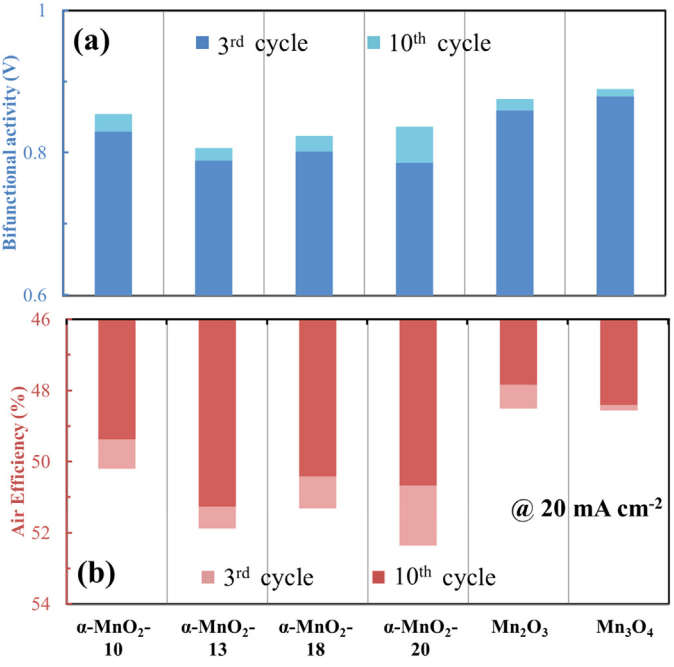

Fig. 9. Evaluation of bifunctional activity and air-efficiency retention at 20 mA cm^{-2} of selected Mn_xO_y catalysts. Dark colors represent the values at the initial state (3rd cycle) and light color after 10 full (OER-ORR) cycles.

With these results it has demonstrated the synthesis of a promising and cheap manganese oxide based catalyst which could be implemented as an alternative cathode material to further improve the current state of zinc-air battery technology. As part of an ongoing R&D work that has as main objective the development of high reversible zinc air battery based on aqueous alkaline electrolyte, further work will include the analysis of other cell components and their effect on the overall battery performance. This will include an optimal BAE engineering process where other non-carbonaceous conductive media (such as Ni or Ag) would be considered. At the same time, and in order to reduce the water consumption or the loss of the active zinc anode due to passivation and/or migration to the cathode, different separators as well as electrolyte formulations to protect the anode would be also assessed.

4. Conclusion

Different valence states and morphologies of Mn_xO_y catalysts were synthetized in order to develop a bifunctional air cathode catalyst for secondary zinc-air battery application. It has shown α-MnO_2 material (produced by acid digestion of Mn_2O_3) as a very promising catalyst in contrast to Mn_2O_3 and Mn_3O_4 (both from thermal treatment of EMD precursor).

The synthesis of different α-MnO_2 was based on changing the ratio of H^+ to Mn_2O_3 by incorporating different amounts of as-prepared Mn_2O_3 to a constant acid concentration with the intention of change the synthesis rate determinate step (disproportionation of Mn(III)) and hence, influence the crystal growing rate. That was done with the idea of inducing changes on either the morphology or the structure of the α-MnO_2.

In general, it has not found any significant influence on the morphology of the as-synthetized α-MnO_2, although, formation of nanowire in comparison to the most usual nanorod was identified. Changes in the ratio H^+ to Mn_2O_3 during the acid digestion affected the sample microporosity and the crystallographic plane distribution (others than 211 plane), as well as affect the physical and chemical adsorbed water which was related to defects, i.e. cation vacancies (Mn^{4+}) and Mn^{3+}. The latter was linked to the electrocatalytic activity of the synthetized α-MnO_2 showing that the best ORR performing catalyst was that with the higher surface water content (associated to material BET surface area) and a (310) surface as the 2nd more contributing plane (after 211). On the other hand, the catalyst with the higher structural water and with (110) and (200) crystallographic planes being the most intensity contributors (after 211) was the most OER active material. In this way, the crystallographic plane distribution (in term of intensities), as well as the sample water content (surface and structural) could be both associated to the observed trends for ORR and OER activities among the synthetized α-MnO_2 samples. These material's characteristics could be relatively easy controlled by the cost-effective acid digestion method via variation of the acid concentration.

Therefore, in this work, it was able to find a relationship between catalyst structure and air-efficiency through a volcano-

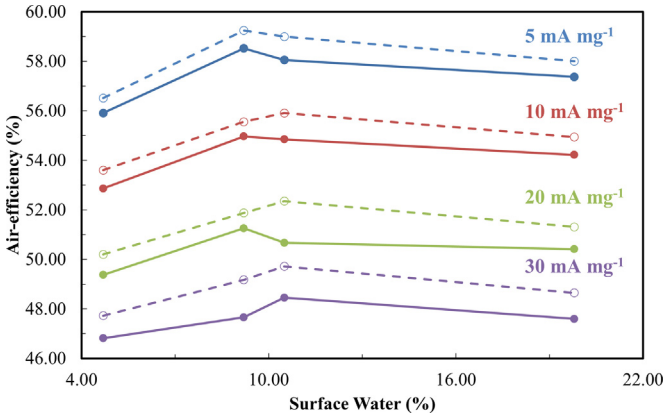

Fig. 10. Relationship between surface water content and air-efficiency at different current densities for selected α-MnO_2 catalysts (close and open circles from left to right in X-axis represent: sample 10, 13, 20 and 18, respectively).

like relationship between air-efficiency and surface water content. Air-efficiency (also taken as round-efficiency discharge/charge in battery context) can be used as a good descriptor of potentially good materials for Zn-Air secondary batteries technology. In this term, we were able to prepare a Bifunctional Air Electrode based on the selected α-MnO_2 sample which support a Zinc-Air battery test showing a round-efficiency of 53%, a ΔV around 1 V and a neglected loss of the charge potential (about 2.1 V) over the entire lifecycle test including more than 200 charge/discharge cycles (over 30 hours) with a capacity retention superior to 95%.

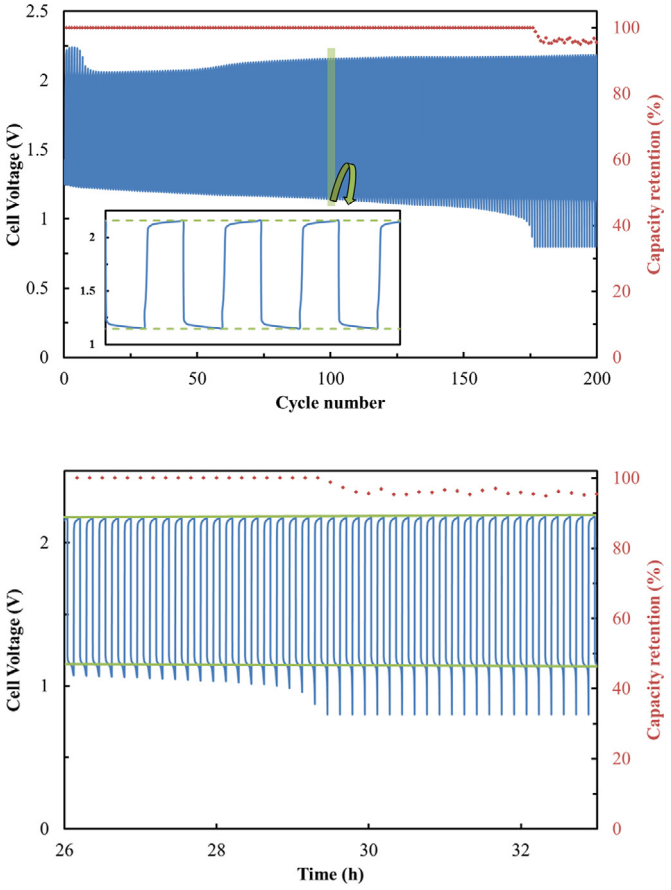

Fig. 11. (a) Charge/discharge cycling (5 min/5 min. Blue solid line) at 10 mAh cm^{-2} for rechargeable Zn-air battery. Red dotted line represents the capacity retention. (b) Stability of the cell overpotential and loss of capacity. The battery consisted of a Zn-foil (50 μm) anode, a separator embedded with the supporting electrolyte (8 M KOH) and the α-MnO_2-13 catalyst/CNF (as conductive media) composite as air electrode. 40 ml min^{-1} synthetic dried air was flowed at the cathode. Voltage cut-off: 0.8 V.

Acknowledgments

This work was supported by the Basque Country University (UPV/EHU) under the program ZABALDUZ2012, the European Commission through the project ZAS: "Zinc Air Secondary innovative nanotech based batteries for efficient energy storage" (Grant Agreement 646186) and by the Basque Country Government (ELKARTEK 2016).

Appendix A. Supplementary data

Supplementary data associated with this article can be found, in the online version, at http://dx.doi.org/10.1016/j.electacta.2016.09.052.

References

[1] Z.-L. Wang, et al., Oxygen electrocatalysts in metal?air batteries: from aqueous to nonaqueous electrolytes, Chem. Soc. Rev. 43 (2014) 7746–7786.
[2] A.R. Mainar, et al., Alkaline aqueous electrolytes for secondary zinc?air batteries: an overview, Int. J. Energy Res. (2016).
[3] P.-C. Li, et al., Synthesis and characterization of carbon black/manganese oxide air cathodes for zinc-air batteries: Effects of the crystalline structure of manganese oxides, J. of Power Sources 298 (2015) 102–113.
[4] Z. Chen, et al., Manganese dioxide nanotube and nitrogen-doped carbon nanotube based composite bifunctional catalyst for rechargeable zinc-air battery, Electrochim. Acta 69 (2012) 295–300.
[5] P.-C. Li, et al., Synthesis and characterization of carbon black/manganese oxide air cathodes for zinc-air batteries: Effects of the crystalline structure of manganese oxides, J. of Power Sources 298 (2015) 102–113.
[6] R.B. Valima, et al., Oxygen reduction reaction catalyzed by e-MnO_2: Influence of the crystalline structure on the reaction mechanism, Electrochim. Acta 85 (2012) 423–431.
[7] F. Cheng, et al., MnO_2-Based Nanostructures as Catalysts for Electrochemical Oxygen Reduction in Alkaline Media, Chem. Mater. 22 (2010) 898–905.
[8] F. Cheng, et al., Enhancing Electrocatalytic Oxygen Reduction on MnO_2 with Vacancies, Angew. Chem. Int. Ed. 52 (2013) 2474–2477.
[9] Q. Tang, et al., Effect of Surface Manganese Valence of Manganese Oxides on the Activity of the Oxygen Reduction Reaction in Alkaline Media, ACS Catal. 4 (2014) 457–463.
[10] W. Xiao, et al., Shape-Controlled Synthesis of MnO_2 Nanostructures with Enhanced Electrocatalytic Activity for Oxygen Reduction, J. Phys. Chem. C 114 (2010) 1694–1700.
[11] Y. Gorlin, et al., In Situ X-ray Absorption Spectroscopy Investigation of a Bifunctional Manganese Oxide Catalyst with High Activity for Electrochemical Water Oxidation and Oxygen Reduction, J. Am. Chem. Soc. 135 (2013) 8525–8534.
[12] Y. Meng, et al., Structure-Property Relationship of Bifunctional MnO_2 Nanostructures: Highly Efficient, Ultra-Stable Electrochemical Water Oxidation and Oxygen Reduction Reaction Catalysts Identified in Alkaline Media, J. Am. Chem. Soc. 136 (2014) 11452–11464.
[13] C.-H. Kuo, et al., Facet-dependent catalytic activity of MnO electrocatalysts for oxygen reduction and oxygen evolution reactions, Chem. Commun. 51 (2015) 5951–5954.
[14] F.H.B. Lima, et al., Electrocatalytic activity of manganese oxides prepared by thermal decomposition for oxygen reduction, Electrochim. Acta 52 (2007) 3732–3738.
[15] K.A. Stoerzinge, et al., Recent Insights into Manganese Oxides in Catalyzing Oxygen Reduction Kinetics, ACS Catal. 5 (2015) 6021–6031.
[16] Y.-J. Huang, et al., Preparation of Manganese Dioxide for Oxygen Reduction in Zinc Air Battery by Hydro thermal Method, J.Inorganic Materials 28 (2013) 341–346.
[17] Y. Gorlin, et al., A Bifunctional Nonprecious Metal Catalyst for Oxygen Reduction and Water Oxidation, J. Am. Chem. Soc. 132 (2010) 13612–13614.
[18] L. Mao, et al., Mechanistic study of the reduction of oxygen in air electrode with manganese oxides as electrocatalysts, Electrochim. Acta 48 (2003) 1015–1021.
[19] H.Y. Lin, et al., Factors influencing the structure of electrochemically prepared a-MnO2 and y-MnO2 phases, Electrochim. Acta 52 (2007) 6548–6553.
[20] T. Poux, et al., Dual role of carbon in the catalytic layers of perovskite/carbon composites for the electrocatalytic oxygen reduction reaction, Catalysis Today 189 (2012) 83–92.
[21] I. Roche, et al., Carbon-Supported Manganese Oxide Nanoparticles as Electrocatalysts for the Oxygen Reduction Reaction (ORR) in Alkaline

Medium: Physical Characterizations and ORR Mechanism, J. Phys. Chem. C 111 (2007) 1434–1443.
[22] M. Komo, et al., Oxygen Evolution and Reduction Reactions on $La_{0.8}Sr_{0.2}CoO_3$ (001) (110), and (111) Surfaces in an Alkaline Solution, Electrochem. Comm. 80 (2012) 834–838.
[23] H.A. Hansen, et al., Surface Pourbaix diagrams and oxygen reduction activity of Pt, Ag and Ni(111) surfaces studied by DFT, Phys. Chem. Chem. Phys. 10 (2008) 3722–3730.
[24] Y. Gorlin, et al., The Role of Heat Treatment in Enhanced Activity of Manganese Oxides for the Oxygen Reduction and Evolution Reactions, ECS Transactions 58 (2013) 735–750.
[25] R.S. Kalubarme, et al., Catalytic characteristics of MnO_2 nanostructures for the O_2 reduction process, Nanotechnology 22 (2011) 395402.
[26] J. Tulloch, et al., Activity of perovskite $La_{1-x}Sr_xMnO_3$ catalysts towards oxygen reduction in alkaline electrolytes, J. Power Sources 188 (2009) 359–366.
[27] S.L. Brock, et al., A Review of Porous Manganese Oxide Materials, Chem. Mater. 10 (1998) 2619–2628.
[28] D.L. Bish, et al., Thermal behavior of complex, tunnel-structure manganese oxides, American Mineralogist 74 (1989) 177–186.
[29] D.K. Walanda, et al., Hydrothermal MnO_2: synthesis, structure, morphology and discharge performance, J. Power Sources 139 (2005) 325–341.
[30] P. Reutschi, et al., Cation Vacancies in MnO_2 and Their Influence on Electrochemical Reactivity, J. Electrochem. Soc.: Electrochemical Science and Technology 135 (1988) 2663–2669.
[31] D.K. Walanda, et al., Kinetics and morphology transformation of manganese oxide in acid electrolyte, Proceeding of The International Seminar on Chemistry (2008) 180–184.
[32] D.K. Walanda, et al., Kinetics of Mn_2O_3 digestion in H_2SO_4 solutions, J. Solid State Chemistry 182 (2009) 1336–1342.
[33] A. Weibel, et al., The Big Problem of Small Particles: A Comparison of Methods for Determination of Particle Size in Nanocrystalline Anatase Powders, Chem. Mater. 17 (2005) 2378–2385.
[34] P. Reutschi, et al., Cation-Vacancy Model for MnO_2: J, Electrochem. Soc.: Electrochemical Science and Technology 131 (1984) 2737–2744.
[35] A. Wieckwski, et al., Fuel cell science. Theory, fundamentals and biocatalysis, Wiley, 2010.
[36] L. Jörissen, Bifunctional oxygen/air electrodes, J. Power Sources 155 (2006) 23–32.
[37] C. de A. Dias, et al., The relation between structural features and electrochemical activity of MnO_2 nanoparticles synthesized from a polyol-made Mn_3O_4 precursor, J. Solid State Electrochem. (2013).
[38] Y. Park, et al., Understanding hydrothermal transformation from Mn_2O_3 particles to $Na_{0.55}Mn_2O_4{\cdot}1.5H_2O$ nanosheets, nanobelts, and single crystalline ultra-long $Na_4Mn_9O_{18}$ nanowires, Nature (2015).
[39] Y.X. Zhang, et al., Hydrothermally Tailoring Low-dimensional MnO_x Nanostructure and Their High Electrochemical Performance, Int. J. Electrochem. Sci. 8 (2013) 2407–2416.
[40] K. Selvakumar, et al., Development of shape-engineered a-MnO_2 materials as bi-functional catalysts for oxygen evolution reaction and oxygen reduction reaction in alkaline medium, Int. J. Hydrogen Energy 39 (2014) 21024–21036.
[41] K. Selvakumar, et al., Physiochemical Investigation of Shape-Designed MnO_2 Nanostructures and Their Influence on Oxygen Reduction Reaction Activity in Alkaline Solution, J. Phys. Chem. C 119 (2015) 6604–6618.
[42] C.S. Johnson, et al., Structural and electrochemical studies of a-manganese dioxide (α-MnO_2), J. Power Sources 68 (1997) 570–577.
[43] B. Prélot, et al., Structural-chemical disorder of manganese dioxides 1. Influence on surface properties at the solid-electrolyte interface, J. Colloid and Interface Science 257 (2003) 77–84.
[44] E.M. Benbow, et al., Oxygen Reduction Properties of Bifunctional α-Manganese Oxide Electrocatalysts in Aqueous and Organic Electrolytes, J. Phys. Chem. C 115 (2011) 22009–22017.
[45] F.Y. Cheng, et al., ACS Appl. Mater. Interfaces 1 (2009) 460.
[46] J. Liu, et al., Activating Mn_3O_4 by Morphology Tailoring for Oxygen Reduction Reaction, Electrochim. Acta 205 (2016) 38–44.
[47] P.H. Benhangi, Manganese Dioxide-based Bifunctional Oxygen Reduction/Evolution Electrocatalysts: Effect of Perovskite Doping and Potassium Ion Insertion, Electrochim. Acta 123 (2014) 42–50.
[48] L.C. Colmenares, et al., Model study on the stability of carbon support materials under polymer electrolyte fuel cell cathode operation conditions, J. Power Sources 190 (2009) 14–24.
[49] V. Neburchilov, et al., A review on air cathodes for zinc-air fuel cells, J. Power Sources 195 (2010) 1271–1291.
[50] S. Suren, et al., Development of a High Energy Density Flexible Zinc-Air Battery, J. Electrochem. Soc. 163 (2016) A846–A850.